Fiducial marker based intra-fraction motion assessment on cine-MR for MR-Linac treatment of prostate cancer

D.M. de Muinck Keizer[a,1,*], A.U. Pathmanathan[b,*], A. Andreychenko[a,c], L.G.W. Kerkmeijer[a], J.R.N. van der Voort van Zyp[a], A.C. Tree[b], C.A.T. van den Berg[a], J.C.J. de Boer[a]

[a] *University Medical Center Utrecht, Department of Radiotherapy, P.O. Box 85500, 3508 GA, Utrecht, The Netherlands*

[b] *Royal Marsden Hospital NHS Foundation Trust and Institute of Cancer Research, Fulham Road, SW3 6JJ, London, UK*

[c] *ITMO University, 49 Kronverksky Pr., St. Petersburg, 197101, Russia*

[*] Joint first author

Email addresses: D.M.deMuinckKeizer@umcutrecht.nl (D.M. de Muinck Keizer), Angela.Pathmanathan@icr.ac.uk (A.U. Pathmanathan), andreychenko.a@gmail.com (A. Andreychenko), L.Kerkmeijer@umcutrecht.nl (L.G.W. Kerkmeijer), J.R.N.vanderVoortvanZyp@umcutrecht.nl (J.R.N. van der Voort van Zyp), Alison.Tree@rmh.nhs.uk (A.C. Tree), C.A.T.vandenBerg@umcutrecht.nl (C.A.T. van den Berg), J.C.J.deBoer-6@umcutrecht.nl (J.C.J. de Boer)

[1] Corresponding author

[2] Word count abstract: 263 of max 300

[3] Word count body: 3691

Abstract

Purpose We have developed a method to determine intrafraction motion of the prostate through automatic fiducial marker (FM) tracking on 3D cine-magnetic resonance (MR) images with high spatial and temporal resolution.
Methods Twenty-nine patients undergoing prostate stereotactic body radiotherapy (SBRT), with four implanted cylindrical gold FMs, had cine-MR imaging sessions after each of five weekly fractions. Each cine-MR examination consisted of 55 sequentially obtained 3D datasets ('dynamics'), acquired over a 11 second period, covering a total of 10 minutes. FM locations in the first dynamic were manually identified by a clinician, FM centers in subsequent dynamics were automatically determined. Center of mass (COM) translations and rotations were determined by calculating the rigid transformations between the FM template of the first and subsequent dynamics. The algorithm was applied to 7315 dynamics over 133 scans of 29 patients and the obtained results were validated by comparing the COM locations recorded by the clinician at the halfway-dynamic (after 5 minutes) and end dynamic (after 10 minutes).
Results The mean COM translations at 10 minutes were X: 0.0±0.8 mm, Y: 1.0±1.9 mm and Z: 0.9±2.0 mm. The mean rotation results at 10 minutes were X: 0.1±3.9°, Y: 0.0±1.3° and Z: 0.1±1.2°. The tracking success rate was 97.7% with a mean 3D COM error of 1.1 mm.
Conclusion We have developed a robust, fast and accurate FM tracking algorithm for cine-MR data, which allows for continuous monitoring of prostate motion during MR-guided radiotherapy (MRgRT). These results will be used to validate automatic prostate tracking based on soft-tissue contrast.

Keywords: prostate cancer, intrafraction motion, hypofractionation, fiducial marker, tracking, cine-MR

1. Introduction

In present-day external beam radiotherapy (RT) for prostate cancer, accurate targeting is often based on kilovoltage (kV) and megavoltage (MV) imaging of implanted gold fiducial markers (FM). The implantation of FM prior to prostate RT allows accurate patient set-up verification prior to each fraction of the treatment [1, 2]. In addition, co-registration of planning computed tomography (CT) and magnetic resonance imaging (MRI) images is more accurate with the use of FM [3]. However although this image-guided RT (IGRT) permits margin reduction [4, 5], online images acquired prior to the RT fraction do not adjust for intrafraction movement of the prostate, which can be significant and is dependent on patient movement, bladder and rectal filling [6–9].

MRI provides several benefits during the RT planning process including increased soft tissue contrast for delineation of the prostate [10–12], seminal vesicles and organs at risk (OAR) without the use of additional radiation exposure. MR-guided systems [13, 14] harness the advantages of MRI for intrafractional imaging with the potential for tumour tracking, gated treatment and adaptive radiotherapy [15]. For these to occur, a realistic assessment of prostate motion is required to determine the planning margins added to the prostate clinical target volume (CTV). Specifically, techniques for fast adaptation to the anatomy of the moment based on continuous MR imaging [16], require reliable motion information to be automatically extracted from the image stream.

Inter- and intrafractional prostate motion has been extensively studied [17, 18]. In particular, the use of cine-MR images can be used to reflect the prostate motion during a treatment fraction with previous studies using defined points of interest [7, 9, 19, 20], the prostate boundaries [8] or measurement of movement compared to a baseline contour [6]. These provide data on drift of the prostate as well as transient movements of varying magnitude, however do not consider the entire prostate volume. Continuous motion data during radiotherapy treatment itself is provided by tracking electromagnetic markers [21] and reporting the frequency and magnitude of displacements using the geometric center of the markers.

FM have become the standard for accurate registration of the prostate

in kV imaging. We therefore first focus on FM tracking in MR images to obtain results that can be compared to the literature. FMs create a high signal on CT images [22] and are therefore easily identified, however, specific sequences are required to visualize FMs properly on MR images such as spin echo, gradient echo and balanced steady-state free precession (bSSFP) sequences imaging [23, 24]. More recent work has focused on automatic FM detection using these sequences [23, 25–28]. There are a number of methods including template matching to detect FM [26, 29], feature extraction from MR intensities [23, 28] or even a combination of approaches [25].

Here we use an extensive dataset of three dimensional (3D) bSSFP cine-MR scans with sufficient temporal resolution to assess the accuracy of an automatic fiducial detection method. We assess the detailed characteristics of prostate motion, including rotations, over the ten minute period of the cine-MR, reflecting the duration of a RT fraction. We have developed the automatic fiducial detection method to obtain ground truth intrafraction motion in preparation of soft-tissue MR-guided RT of the prostate. To our knowledge, this is the first data using automatic FM tracking on cine-MR to assess intrafraction motion. The obtained results will be used in the development of a FM-free soft-tissue tracking method of the prostate.

2. Materials and Methods

Patient selection

Twenty-nine patients undergoing prostate SBRT within the HypoFLAME trial (NCT02853110) with four implanted cylindrical gold FM (5 mm length, 1 mm diameter), had repeated cine-MR imaging sessions at the University Medical Center Utrecht after each of five weekly fractions. During these imaging sessions, patient set-up was similar to that during prostate RT. Apart from drinking 400 ml water prior to scanning or treatment, no specific rectal or bladder preparations were applied.

Image acquisition

Each cine-MR examination consisted of 55 sequentially obtained 3D datasets (dynamics) that were acquired with a 3D bSSFP sequence using fat suppression (repetition time (TR)=4 ms, echo time (TE)=1.98 ms, flipangle=30°, B_0=3T) that provided good anatomical as well as FM contrast. Each dynamic was acquired over a 11 second period, with a voxel size of 0.96x0.96x2

mm^3 and a 384x384x120 mm^3 field of view. Each cine-MR exam therefore covered a 10 minute period.

Manual FM identification

The locations of the FM in the first dynamic were manually determined by a clinician, who marked the top and bottom location of each FM according to the method described by Maspero et al. [24], from which the FM center was obtained. The FM template containing the 3D-positions of all markers on the first dynamic was then stored. An example of manually segmented markers on cine-MR images is provided in Figure 1. The marking of the FM top and bottom was performed without reference to the CT of the patient. The found marker template of the FM by the clinician was compared with available FM templates obtained from CT scans of the patients. The FM centers in subsequent dynamics were automatically determined using in-house developed Python code as described in the next section.

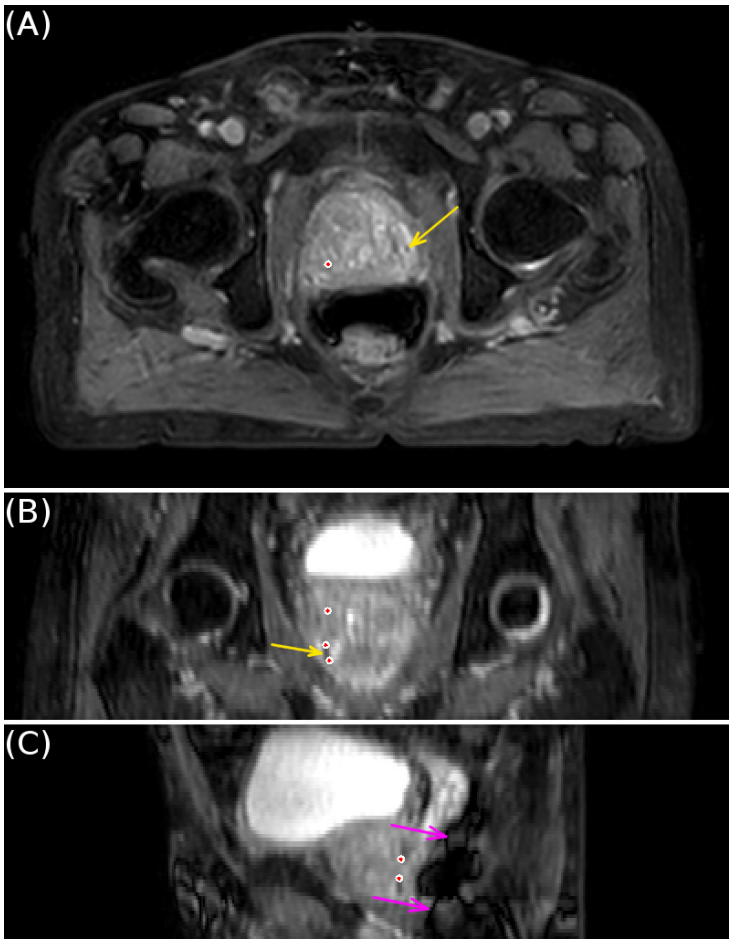

Figure 1: Overview of cine-MR images with manually segmented markers by the clinician. Images A, B and C show the respectively transversal, coronal and sagittal slices of a patient. Manually segmented marker top or bottom locations are visualized as the dots. The (yellow) arrows in image A and B show the effect of a signal void caused by a fiducial marker. The highlighted signal void in image A has no dot as this void is in the center of a marker located in the cranial-caudal plane. The effect of the banding artifact caused by rectal gas is highlighted by the (magenta) arrows in image C.

Automatic FM identification

All dynamics were resampled to a voxel spacing of 0.25 mm^3 to improve the accuracy and resolution of the automatic tracking results. Automatic determination of the FMs in subsequent frames was then performed by defining a local kernel of voxels with a diameter of 7 mm and height of 14 mm around each fiducial center in the first dynamic. The defined kernels were individ-

ually correlated to subsequent dynamics using the Pearson correlation to determine the current location of all FM, in a radius of 15 mm around the initial FM position of the first dynamic.

To reduce the influence of outliers from wrongly determined FM locations and increase robustness, the found FM locations of all subsequent dynamics were rigidly mapped to the marker template of the first dynamic using a leave-one-out strategy. All four possible combinations of three markers from the current dynamic were used to calculate a rigid transformation to the marker template of the first dynamic. The transformation with the lowest intra-marker difference between the mapped and original FM points was used for the determination of the final Euler transformation. The calculated transformation is thus based on three markers and describes the translation and rotation between the first and current dynamic and these variables are stored as the center of mass (COM) translation and rotation.

The results from the algorithm were verified by comparing the automatically found COM locations with the locations manually identified by the clinician at the halfway (27th) dynamic (after approximately 5 minutes) and end (55th) dynamic (after approximately 10 minutes). The grid system used in this paper defines X as left-right (where positive denotes right), Y as anterior-posterior (where positive denotes posterior) and Z as the caudal-cranial axis (where positive denotes cranial).

Statistics

Different statistical analyses were used to assess the results. The analyzed statistical metrics include the systematic error per patient per time point, the group mean displacement per time point, population systematical error per time point and the population random error per time point. The systematical error per patient (Sp) can be seen as the mean error over the patient's treatment, and is calculated on time point t_i by:

$$S_p(t_i) = \frac{1}{N_c(p)} \sum_{c=1}^{N_c(p)} \Delta_{p,c}(t_i) \tag{1}$$

With $N_c(p)$ as the number of total cine-MR scans per patient (p), c as the cine-MR scan number and Δ as the translation per direction in X, Y or Z. The group mean displacement (M) on time point t_i can then be calculated

with:

$$M(t_i) = \frac{1}{N_p} \sum\nolimits_{p=1}^{N_p} S_p(t_i) \tag{2}$$

With N_p as the total number of included patients. Using equation 1 and 2, the population systematical error can be seen as a measure for the mean displacement in all patients and is calculated by:

$$\Sigma(t_i) = \left(\frac{1}{N_p - 1} \sum\nolimits_{p=1}^{N_p} \Big(S_p(t_i) - M(t_i) \Big)^2 \right)^{1/2} \tag{3}$$

The population random error is calculated by using:

$$\sigma(t_i) = \left(\frac{1}{N_p} \sum\nolimits_{p=1}^{N_p} \frac{1}{N_c(p) - 1} \sum\nolimits_{c=1}^{N_c(p)} \Big(\Delta_{p,c}(t_i) - S_p(t_i) \Big)^2 \right)^{1/2} \tag{4}$$

The population random error can be denoted as the effective random displacement, as it provides a measure for the mean fluctuations in the found result of the population [30].

The algorithm's success rate was determined by calculating the mean absolute intramarker distance between the FMs found in the current dynamic, and the FMs of the first dynamic, transformed to the current dynamic. The transformation of the FMs from the first to the current dynamic was performed by applying the inverse of the obtained transformation between the current and first dynamic. The intramarker distance was defined as the difference between the found position of a FM in the current dynamic and the transformed position of the same FM from the first to the current dynamic. If the mean absolute intramarker distance was equal to or less than 0.25 mm (equal to the resampled voxel spacing), the identification of the individual FMs and the registration between the dynamics was considered a success.

3. Results

The algorithm was applied to 7315 dynamics over 133 scans of 29 patients and a graphical representation of these results is summarized in Figure 2 and Figure 3. Figure 2 provides an overview of the population mean translation results. The population mean rotation results are provided in Figure 3. Patients spent on average 2.4±0.7 minutes on the scanner table before the start of the cine-MR imaging sequence. The mean 3D error in the COM position

found by the algorithm compared with the clinician on dynamic 27 and 55 is 1.1±0.7 mm with the largest 3D error being 3.8 mm. The mean 3D error in the FM positions provided by the clinician based on MR images compared with the 3D positions obtained from CT scans is 1.6±1.2 mm. Linear regression analysis between the COM of the validation points by the clinician and the found COM positions by the algorithm returned a correlation value of 0.92. The success rate of the algorithm's tracking and registration was 97.7%.

The found COM translations at 10 minutes were 0.0±0.8 mm (maximum 3.4 mm) for X, 1.0±1.9 mm (maximum 9.7 mm) for Y (posterior direction) and 0.9±2.0 mm (maximum 8.0 mm) for Z (caudal direction). The rotation results at 10 minutes were 0.1±3.9° (maximum 30.3°) for X (towards anterior), 0.0±1.3° (maximum 4.0°) for Y and 0.1±1.2° (maximum 3.8°) for Z. Cumulative 3D translation occurrences of the COM of at least 2, 4 and 5 mm are provided in Figure 4. These results indicate the cumulative fraction of scans in which the 3D COM translation was larger than the thresholds from the start of the imaging sequence up to the time intervals of 1, 3, 5, 7, 9 and 10 minutes. Results on the cumulative occurrences of COM rotations of at least 2, 4 and 5 degrees in the X direction are presented in Figure 5. Figure 6 provides an overview of the population systematic translation error. The population random translation error is given in Figure 7. An overview of individual motion paths of a single imaging session of a patient is given in Figure 8. The graphs show the difference in results for the cases when using three markers versus all four markers.

Full automatic analysis of a single dynamic took 10 seconds, which is sufficiently fast to analyze an incoming cine-MR data stream without lag.

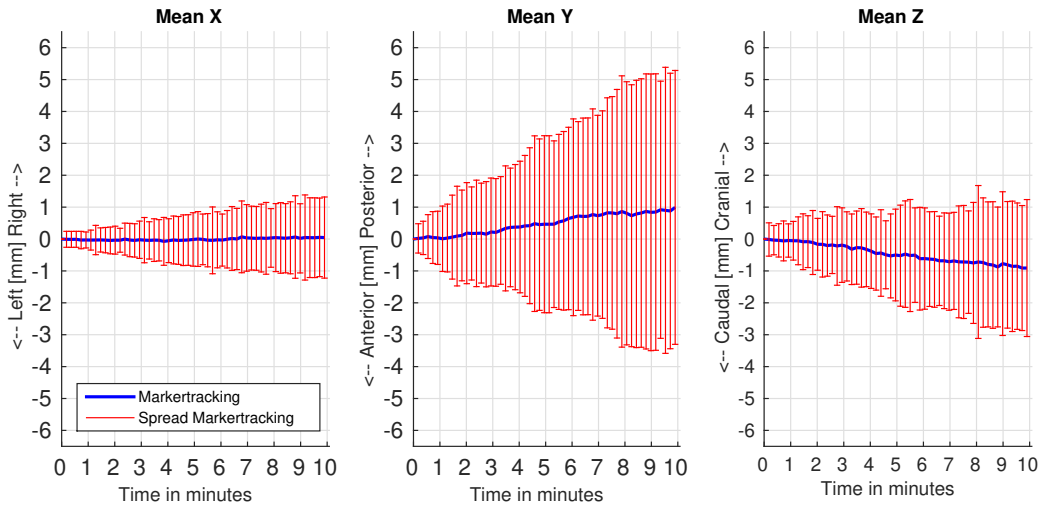

Figure 2: Overview of the population translation results, which show the found translation trends of 1 mm in the posterior and 0.9 mm in the caudal direction with the found spread (95 percentile) at each time point (over patients and fractions) as error bars. No translation trend was observed for the left-right direction.

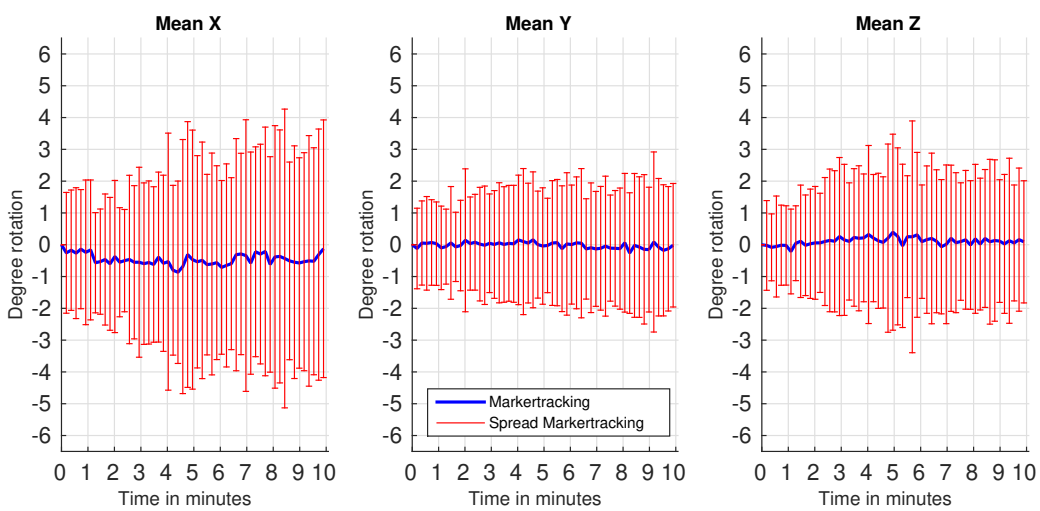

Figure 3: Overview of the population rotation results. The mean anterior-posterior rotation (about the X-axis) is provided on the left hand side and shows a small mean rotation trend of 0.5 degree in the anterior direction during the 10 minute time period with the found spread (95 percentile) at each time point (over patients and fractions) as error bars. No rotational trend was observed for the Y and Z axis.

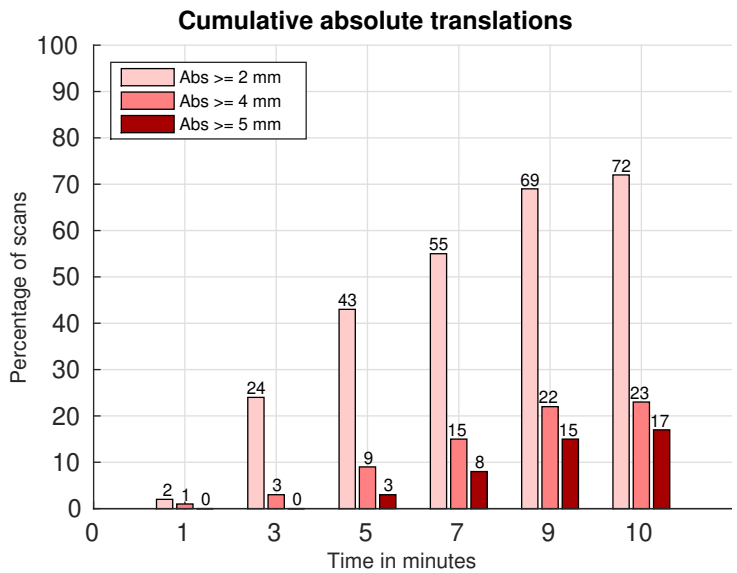

Figure 4: Overview of the cumulative percentage of scans, in which the found 3D COM translations is at least 2, 4 or 5 mm.

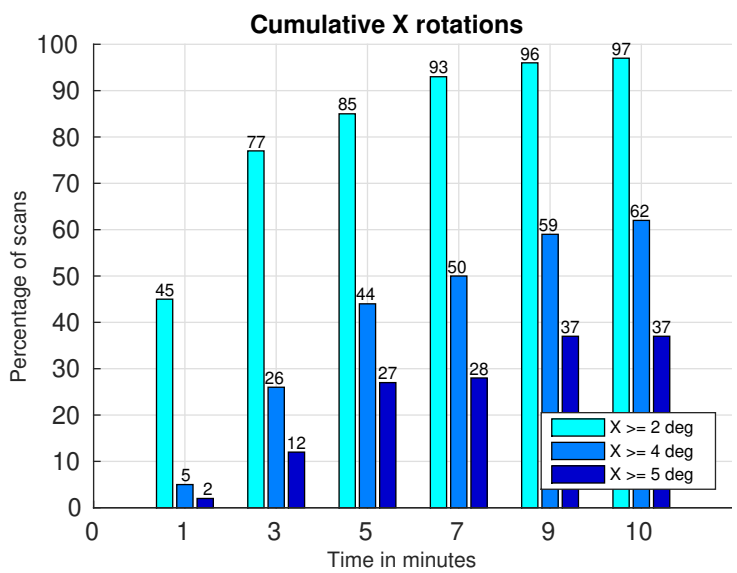

Figure 5: Overview of the cumulative percentage of scans, in which the found X rotation is at least 2, 4 or 5 degrees.

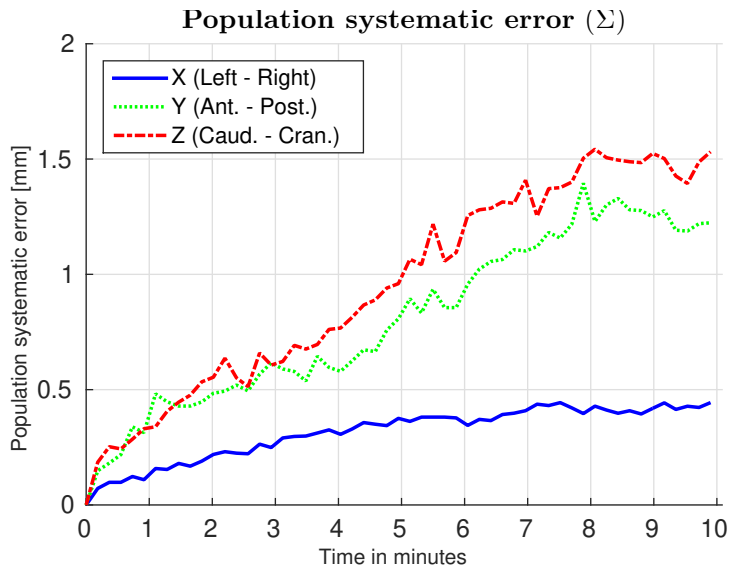

Figure 6: The development of the systematic translation errors (Σ) over time, for the three main directions.

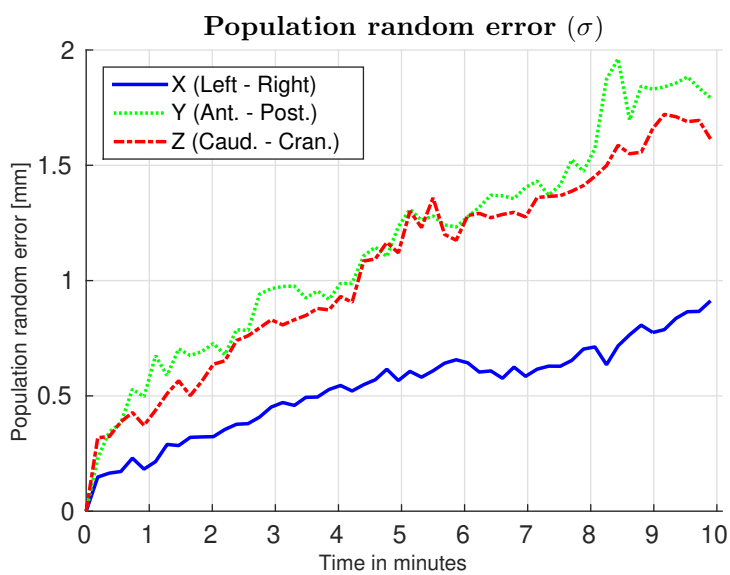

Figure 7: The development of the random translation errors (σ) over time, for the three main directions.

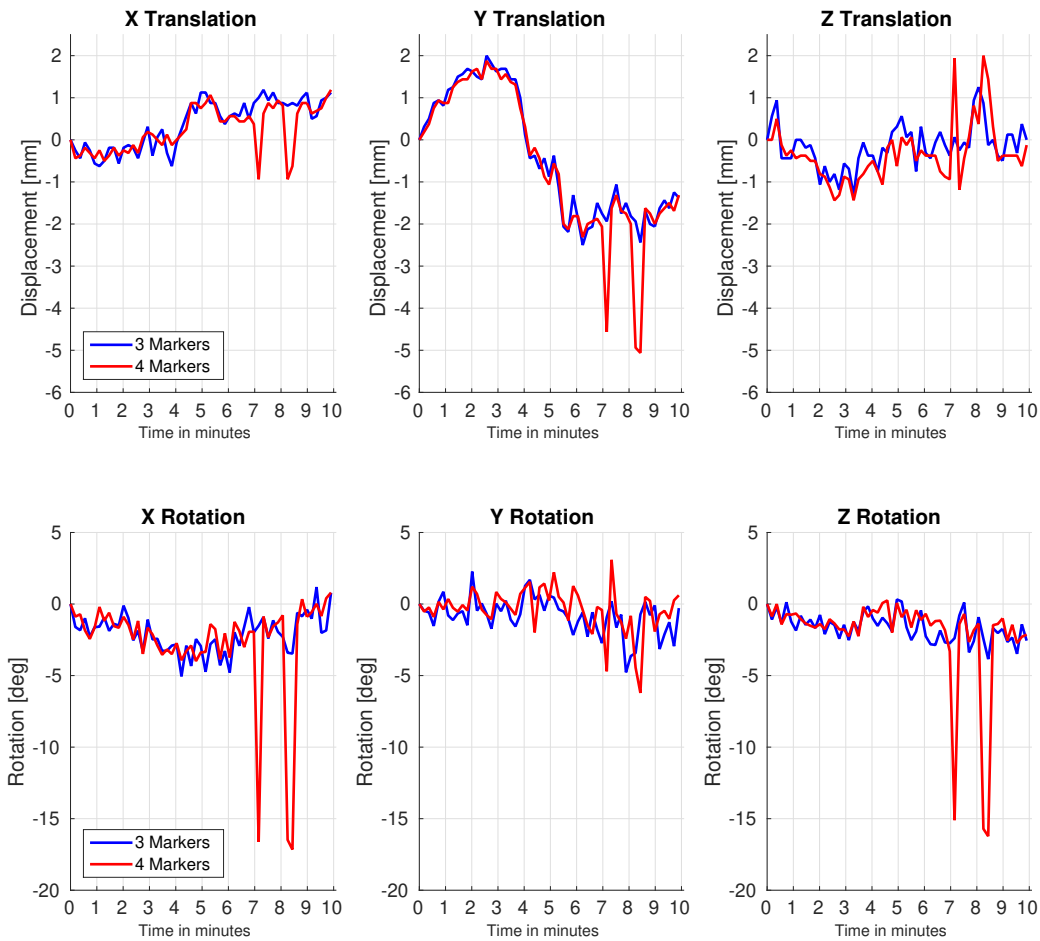

Figure 8: Overview of individual motion paths during a single imaging session of a patient. The results are shown for the case when using the best three markers (blue), and using all four markers (red). From the X and Z rotation graphs can be observed that using all four markers can result in large rotation values.

4. Discussion

Linear regression analysis indicated a good agreement between the COM of the validation points by the clinician and the found COM positions by the algorithm. To our knowledge, this is the first fully 3D cine-MR analysis of prostate intrafraction motion. This makes comparison to literature difficult and we can only compare to algorithms which are optimized for automatic fiducial marker detection in non-cine-MR sequences. An example of automatic fiducial detection is described by Ghose et al. who reported a mean centroid difference of 0.5±0.5 mm while using a voxel spacing of 0.6x0.6x2 mm with non-cine-MR sequences specifically optimized for FM detection [25]. The success rate of our tracking method for registrations was 97.7% based on an independent conservative measure as described in the material and methods section. On the other hand, we have detected prostate intrafraction motion of up to 9.7 mm, significantly larger than the obtained 3D error of 1.1±0.7 mm. Therefore, the accuracy of our tracking method is sufficient for clinical application.

While using three instead of all four available FM may seem sub-optimal at first, determining the Euler transformation on the best three fitting markers to the marker template of the first dynamic result in lower errors for the found translation and rotation. All FM are individually tracked and used to determine the rigid Euler transformation. Therefore, a single wrongly localized marker can result in particularly large rotation errors as shown in Figure 8. In this figure, large rotation values can be observed for the X and Z rotation when using four markers around the 7 and 8.5 minutes mark. To reduce the influence of outliers and obtain robust motion results, the three best fitting markers to the marker template of the first dynamic were used to obtain the translation and rotation motion.

A marker tracking simulation was performed to identify the effect of single voxel marker mis-locations in the anterior-posterior direction on the obtained rotation results. In this simulation, a fiducial marker model was used based on the group mean fiducial marker positions of all patients, obtained from the CT scan of patients. The simulation showed that the marker tracking left-right rotation results have a mean measurement step size of 0.67 degrees.

Two scans were excluded from the analysis based on visual inspection

of the cine-MR data and the performance of the marker tracking algorithm. These scans were excluded due to an excessive banding artifact caused by local B_0 distortions due to rectal gas and are typical for bSSFP sequences. The banding artifact overlapped on large portions of the prostate, which made it nearly impossible to find marker locations in the prostate with confidence. The effect of the banding artifact is shown in Figure 1, image C. Fernandes et al. [23] had previously reported the impact on fiducial detection of gas within the rectum causing a signal drop-off. Use of a different MR sequence (e.g. spoiled gradient echo) in future image acquisition can help to eliminate the influence of banding artifacts. Apart from these rare artifacts, we have shown that fast and accurate FM tracking on 3D cine-MR is feasible and may be applied on an MR-linac.

A maximum 3D error of 3.8 mm in the COM position found by the algorithm compared with the clinician was found. This error is visualized in Figure 9 and Figure 10 in the supplementary material. In this particular case, two markers were identified which were placed relatively close together in the prostate. Further inspection showed that the signal void of both markers seemed to partially overlap in the cranial-caudal direction. It is a possibility that the clinician segmented the markers differently in the first dynamic, from which the template for the marker tracking is extracted. The error of 3.8 mm could then originate from deviations in the manual segmentations. An investigation with multiple observers could specify if this is the case, or that the difference originates from an error in the algorithm.

The population results in Figure 2 and Figure 3 show that the magnitude of intrafraction displacements continuously increased over the 10 minute interval. Next to the small overall trends, the spread of the displacements increased consistently. The growth of the displacements is visualized by the figures and suggests that the prostate will continue to move after 10 minutes, consistent with the random walk model of Ballhausen et al [31].

Figure 4 shows that the translations continue to increase over time, which is also reflected by Figure 2. A majority of the scans (72%) showed a COM translation of at least 2 mm during the 10 minutes, while a COM translation of at least 5 mm was found in 17% of the scans during the 10 minutes. Only the X rotations were shown in Figure 5, as significant rotations about the X-axis were most commonly observed. More than one-third of the scans (37%)

showed a X rotation of at least 5 degrees during the 10 minutes. Z and Y rotations are less common with at least 5 degrees Z rotation in 9% and at least 5 degrees Y rotation in 3% of the scans during the 10 minutes. The maximum X rotation of 30.3° was found in a case where a gas pocket passing by caused severe intrafraction motion in the period of a single dynamic.

The presented results are consistent with published results. Results from this research reflect that the largest rotation occurs about the left-right (LR) axis, while the translation motions are mainly found in the anterior-posterior (AP) and cranial-caudal (CC) direction [6, 8, 32, 33]. The population average trends can be described as a group mean displacement of 1 mm in both the posterior and caudal direction and an 0.5 degree rotational trend in the anterior direction over the X axis over a 10 minute time period. This may be due to a gradual increase in bladder filling. The effect of breathing on prostate intrafraction motion was not taken into account, as influence of breathing on prostate motion was found to be very small [19]. When considering prostate displacements, both the magnitude and duration are relevant. Our findings of increased movement over time are consistent with tracking data from electromagnetic markers [21, 34], cine-MR studies [7] and transperineal ultrasound imaging [33]. As stated before, our findings indicate a monotonously increasing displacement with an increasing variance over time, consistent with findings reported in literature [31]. Similar results obtained with the Calypso Localization System over an 8 minute time period are reported by Olsen et al. [35], where the findings indicate prostate displacement trends in the Y (0.64±0.5 mm) and Z (0.96±0.6 mm) direction and rotation over the X axis (5.7±5°). Huang et al. [36] reported an X-axis rotation of at least 5 degrees in 35% of all scans at 8 minutes time interval, in agreement with our findings. Comparable motion characteristics within the same order of magnitude have been reported by other groups [37–39].

Clearly, a shorter treatment time results in less prostate motion and so effort should be put in reducing time between patient positioning and treatment if no strategies for countering intrafraction motion are available. This claim is supported by Ballhausen et al. [40] who found that the 3D prostate displacement significantly reduced from 1.31±1.28 mm for intensity modulated radiotherapy (IMRT) at 6 minutes to 0.96±1.04 mm for volumetric arc therapy (VMAT) of under 3 minutes. Similar conclusions were reported by Cramer et al. [34], who advise to reposition the patient for treatment dura-

tions over 4-6 minutes when no correction protocol for intrafraction motion is used. However, the picture dramatically changes if cine-MR data will be used to drive real-time plan adaptation on an MR-linac [16, 41]. Then, in principle, overall treatment time will not be vital anymore to treatment accuracy but only to patient comfort and treatment costs. The cine-MR datasets analysed here incorporate a ten minute period, with the aim of representing the duration of treatment delivery. With the recent implementation of MR-guided radiotherapy at our institutions, the workflow encompasses acquiring daily MRI and online re-planning. The patient is therefore on the treatment couch for a longer duration, however repeat verification imaging is carried out prior to treatment delivery to ensure the coverage of the prostate remains adequate. The data we have presented here remains highly relevant, as the evaluation of prostate motion during the MR-guided workflow is paramount, particularly with the aim of real-time adaptive radiotherapy during treatment delivery in the future. In addition, using FM tracking will just be a first step in this process as the full potential of 3D cine-MR data for soft-tissue tracking and hence optimal dose adaptation can then be exploited.

Therefore, our next aim is soft tissue motion monitoring of the prostate, without the use of FM. Our current research therefore involves the development of a FM-free tracking method of the prostate, where the results of the presented study will be used for validation.

5. Conclusion

We have developed a robust, fast and accurate FM tracking algorithm in cine-MR data, which allows for continuous monitoring of intrafraction motion and validation of FM-free soft-tissue tracking methods in MR-guided radiotherapy. As stated before, to our knowledge this is the first data using automatic FM tracking on cine-MR to assess prostate intrafraction motion. We obtained six degrees of freedom prostate intrafraction motion based on volumetric cine-MR images only. The results include rotational analysis for which there is considerably less data available in literature than prostate translation. We found a continuous increase with time in intrafraction motion magnitude (translations and rotations) over a ten minute period, which hardly flattened. The amplitude and temporal behavior of the found intrafraction motion stresses the importance of real-time MR-guidance by fast imaging and dose re-optimization for prostate SBRT.

6. Acknowledgements

This paper represents independent research support by the National Institute for Health Research (NIHR) Biomedical Research Centre at the Royal Marsden NHS Foundation Trust and the Institute of Cancer Research. The views expressed are those of the author(s) and not necessarily those of the NHS, the NIHR or the Department of Health.

[1] U. A. van der Heide, A. N. Kotte, H. Dehnad, P. Hofman, J. J. Lagenijk, M. van Vulpen, Analysis of fiducial marker-based position verification in the external beam radiotherapy of patients with prostate cancer, Radiotherapy and Oncology 82 (1) (2007) 38–45.

[2] T. F. Mutanga, H. C. de Boer, V. Rajan, M. L. P. Dirkx, L. Incrocci, B. J. Heijmen, Day-to-day reproducibility of prostate intrafraction motion assessed by multiple kV and MV imaging of implanted markers during treatment, International Journal of Radiation Oncology* Biology* Physics 83 (1) (2012) 400–407.

[3] C. C. Parker, A. Damyanovich, T. Haycocks, M. Haider, A. Bayley, C. N. Catton, Magnetic resonance imaging in the radiation treatment planning of localized prostate cancer using intra-prostatic fiducial markers for computed tomography co-registration, Radiotherapy and Oncology 66 (2) (2003) 217–224.

[4] C. Beltran, M. G. Herman, B. J. Davis, Planning target margin calculations for prostate radiotherapy based on intrafraction and interfraction motion using four localization methods, International Journal of Radiation Oncology* Biology* Physics 70 (1) (2008) 289–295.

[5] D. W. Litzenberg, J. M. Balter, S. W. Hadley, H. M. Sandler, T. R. Willoughby, P. A. Kupelian, L. Levine, Influence of intrafraction motion on margins for prostate radiotherapy, International Journal of Radiation Oncology* Biology* Physics 65 (2) (2006) 548–553.

[6] A. R. Padhani, V. S. Khoo, J. Suckling, J. E. Husband, M. O. Leach, D. P. Dearnaley, Evaluating the effect of rectal distension and rectal movement on prostate gland position using cine MRI, International Journal of Radiation Oncology* Biology* Physics 44 (3) (1999) 525–533.

[7] M. J. Ghilezan, D. A. Jaffray, J. H. Siewerdsen, M. Van Herk, A. Shetty, M. B. Sharpe, S. Z. Jafri, F. A. Vicini, R. C. Matter, D. S. Brabbins, et al., Prostate gland motion assessed with cine-magnetic resonance imaging (cine-MRI), International Journal of Radiation Oncology* Biology* Physics 62 (2) (2005) 406–417.

[8] D. Mah, G. Freedman, B. Milestone, A. Hanlon, E. Palacio, T. Richardson, B. Movsas, R. Mitra, E. Horwitz, G. E. Hanks, Measurement of intrafractional prostate motion using magnetic resonance imaging, International Journal of Radiation Oncology* Biology* Physics 54 (2) (2002) 568–575.

[9] I. Ogino, T. Kaneko, R. Suzuki, T. Matsui, S. Takebayashi, T. Inoue, S. Morita, Rectal content and intrafractional prostate gland motion assessed by magnetic resonance imaging, Journal of Radiation Research 52 (2) (2011) 199–207.

[10] V. S. Khoo, A. R. Padhani, S. F. Tanner, D. J. Finnigan, M. O. Leach, D. P. Dearnaley, Comparison of MRI with CT for the radiotherapy planning of prostate cancer: a feasibility study., The British Journal of Radiology 72 (858) (1999) 590–597.

[11] G. M. Villeirs, K. Van Vaerenbergh, L. Vakaet, S. Bral, F. Claus, W. J. De Neve, K. L. Verstraete, G. O. De Meerleer, Interobserver delineation variation using CT versus combined CT+MRI in intensity–modulated radiotherapy for prostate cancer, Strahlentherapie und Onkologie 181 (7) (2005) 424–430.

[12] C. Rasch, I. Barillot, P. Remeijer, A. Touw, M. van Herk, J. V. Lebesque, Definition of the prostate in CT and MRI: a multi-observer study, International Journal of Radiation Oncology* Biology* Physics 43 (1) (1999) 57–66.

[13] B. W. Raaymakers, J. J. Lagendijk, J. Overweg, J. G. Kok, A. J. Raaijmakers, E. M. Kerkhof, R. W. Van Der Put, I. Meijsing, S. P. Crijns, F. Benedosso, et al., Integrating a 1.5 T MRI scanner with a 6 MV accelerator: proof of concept, Physics in Medicine & Biology 54 (12) (2009) N229.

[14] S. Mutic, J. F. Dempsey, The Viewray system: magnetic resonance–guided and controlled radiotherapy, Seminars in Radiation Oncology 24 (3) (2014) 196–199.

[15] A. U. Pathmanathan, N. J. van As, L. G. Kerkmeijer, J. Christodouleas, C. A. Lawton, D. Vesprini, U. A. van der Heide, S. J. Frank, S. Nill, U. Oelfke, et al., Magnetic resonance imaging-guided adaptive radiation therapy: A game changer for prostate treatment?, International Journal of Radiation Oncology* Biology* Physics 100 (2) (2018) 361–373.

[16] C. Kontaxis, G. H. Bol, L. G. Kerkmeijer, J. J. Lagendijk, B. W. Raaymakers, Fast online replanning for interfraction rotation correction in prostate radiotherapy, Medical Physics 44 (10) (2017) 5034–5042.

[17] A. J. McPartlin, X. Li, L. E. Kershaw, U. Heide, L. Kerkmeijer, C. Lawton, U. Mahmood, F. Pos, N. van As, M. van Herk, et al., MRI-guided prostate adaptive radiotherapy–a systematic review, Radiotherapy and Oncology 119 (3) (2016) 371–380.

[18] K. Langen, D. Jones, Organ motion and its management, International Journal of Radiation Oncology* Biology* Physics 50 (1) (2001) 265–278.

[19] K. Terashima, K. Nakamura, Y. Shioyama, T. Sasaki, S. Ohga, T. Nonoshita, T. Yoshitake, K. Atsumi, K. Asai, M. Hirakawa, et al., Can a belly board reduce respiratory-induced prostate motion in the prone position? -assessed by cine-magnetic resonance imaging, Technology in Cancer Research & Treatment 12 (5) (2013) 447–453.

[20] A. M. Nichol, P. R. Warde, G. A. Lockwood, A. K. Kirilova, A. Bayley, R. Bristow, J. Crook, M. Gospodarowicz, M. McLean, M. Milosevic, et al., A cinematic magnetic resonance imaging study of milk of magnesia laxative and an antiflatulent diet to reduce intrafraction prostate motion, International Journal of Radiation Oncology* Biology* Physics 77 (4) (2010) 1072–1078.

[21] K. M. Langen, T. R. Willoughby, S. L. Meeks, A. Santhanam, A. Cunningham, L. Levine, P. A. Kupelian, Observations on real-time prostate gland motion using electromagnetic tracking, International Journal of Radiation Oncology* Biology* Physics 71 (4) (2008) 1084–1090.

[22] E. Meyer, R. Raupach, M. Lell, B. Schmidt, M. Kachelrieß, Normalized metal artifact reduction (nmar) in computed tomography, Medical Physics 37 (10) (2010) 5482–5493.

[23] C. D. Fernandes, C. V. Dinh, M. J. Steggerda, L. C. ter Beek, M. Smolic, L. D. van Buuren, F. J. Pos, U. A. van der Heide, Prostate fiducial marker detection with the use of multi-parametric magnetic resonance imaging, Physics and Imaging in Radiation Oncology 1 (2017) 14–20.

[24] M. Maspero, P. R. Seevinck, N. J. Willems, G. G. Sikkes, G. J. de Kogel, H. C. de Boer, J. R. van der Voort van Zyp, C. A. van den Berg, Evaluation of gold fiducial marker manual localisation for magnetic resonance-only prostate radiotherapy, Radiation Oncology 13 (1) (2018) 105.

[25] S. Ghose, J. Mitra, D. Rivest-Hénault, A. Fazlollahi, P. Stanwell, P. Pichler, J. Sun, J. Fripp, P. B. Greer, J. A. Dowling, MRI-alone radiation therapy planning for prostate cancer: Automatic fiducial marker detection, Medical Physics 43 (5) (2016) 2218–2228.

[26] M. Maspero, C. A. van den Berg, F. Zijlstra, G. G. Sikkes, H. C. de Boer, G. J. Meijer, L. G. Kerkmeijer, M. A. Viergever, J. J. Lagendijk, P. R. Seevinck, Evaluation of an automatic MR-based gold fiducial marker localisation method for MR-only prostate radiotherapy, Physics in Medicine & Biology 62 (20) (2017) 7981–8002.

[27] N. Schieda, L. Avruch, W. M. Shabana, S. C. Malone, Multi-echo gradient recalled echo imaging of the pelvis for improved depiction of brachytherapy seeds and fiducial markers facilitating radiotherapy planning and treatment of prostatic carcinoma, Journal of Magnetic Resonance Imaging 41 (3) (2015) 715–720.

[28] C. Gustafsson, J. Korhonen, E. Persson, A. Gunnlaugsson, T. Nyholm, L. E. Olsson, Registration free automatic identification of gold fiducial markers in MRI target delineation images for prostate radiotherapy, Medical Physics 44 (11) (2017) 5563–5574.

[29] F. Zijlstra, M. A. Moerland, J. R. van der Voort van Zyp, J. L. Noteboom, M. A. Viergever, P. R. Seevinck, Challenges in MR-only seed localization for postimplant dosimetry in permanent prostate brachytherapy, Medical Physics 44 (10) (2017) 5051–5060.

[30] H. C. de Boer, B. J. Heijmen, eNAL: an extension of the NAL setup correction protocol for effective use of weekly follow-up measurements, International Journal of Radiation Oncology* Biology* Physics 67 (5) (2007) 1586–1595.

[31] H. Ballhausen, M. Li, N. Hegemann, U. Ganswindt, C. Belka, Intra-fraction motion of the prostate is a random walk, Physics in Medicine & Biology 60 (2) (2014) 549.

[32] E. Huang, L. Dong, A. Chandra, D. A. Kuban, I. I. Rosen, A. Evans, A. Pollack, Intrafraction prostate motion during imrt for prostate cancer, International Journal of Radiation Oncology* Biology* Physics 53 (2) (2002) 261–268.

[33] D. S. K. Sihono, M. Ehmann, S. Heitmann, S. von Swietochowski, M. Grimm, J. Boda-Heggemann, F. Lohr, F. Wenz, H. Wertz, Determination of intrafraction prostate motion during external beam radiation therapy with a transperineal 4-dimensional ultrasound real-time tracking system, International Journal of Radiation Oncology* Biology* Physics 101 (1) (2018) 136–143.

[34] A. K. Cramer, A. G. Haile, S. Ognjenovic, T. S. Doshi, W. M. Reilly, K. E. Rubinstein, N. Nabavizadeh, T. Nguyen, L. Z. Meng, M. Fuss, et al., Real-time prostate motion assessment: image-guidance and the temporal dependence of intra-fraction motion, BMC Medical Physics 13 (1) (2013) 4.

[35] J. R. Olsen, C. E. Noel, K. Baker, L. Santanam, J. M. Michalski, P. J. Parikh, Practical method of adaptive radiotherapy for prostate cancer using real-time electromagnetic tracking, International Journal of Radiation Oncology* Biology* Physics 82 (5) (2012) 1903–1911.

[36] C.-Y. Huang, J. N. Tehrani, J. A. Ng, J. Booth, P. Keall, Six degrees-of-freedom prostate and lung tumor motion measurements using kilovoltage intrafraction monitoring, International Journal of Radiation Oncology* Biology* Physics 91 (2) (2015) 368–375.

[37] J. N. Tehrani, R. T OBrien, P. R. Poulsen, P. Keall, Real-time estimation of prostate tumor rotation and translation with a kV imaging

system based on an iterative closest point algorithm, Physics in Medicine & Biology 58 (23) (2013) 8517.

[38] T. R. Willoughby, P. A. Kupelian, J. Pouliot, K. Shinohara, M. Aubin, M. Roach, L. L. Skrumeda, J. M. Balter, D. W. Litzenberg, S. W. Hadley, et al., Target localization and real-time tracking using the Calypso 4D localization system in patients with localized prostate cancer, International Journal of Radiation Oncology* Biology* Physics 65 (2) (2006) 528–534.

[39] J. S. Li, L. Jin, A. Pollack, E. M. Horwitz, M. K. Buyyounouski, R. A. Price, C.-M. Ma, Gains from real-time tracking of prostate motion during external beam radiation therapy, International Journal of Radiation Oncology* Biology* Physics 75 (5) (2009) 1613–1620.

[40] H. Ballhausen, M. Li, U. Ganswindt, C. Belka, Shorter treatment times reduce the impact of intra-fractional motion, Strahlentherapie und Onkologie (2018) 1–11.

[41] C. Kontaxis, G. Bol, B. Stemkens, M. Glitzner, F. M. Prins, L. G. Kerkmeijer, J. J. Lagendijk, B. W. Raaymakers, Towards fast online intrafraction replanning for free-breathing stereotactic body radiation therapy with the MR-linac, Physics in Medicine & Biology 62 (18) (2017) 7233.

7. Supplementary material

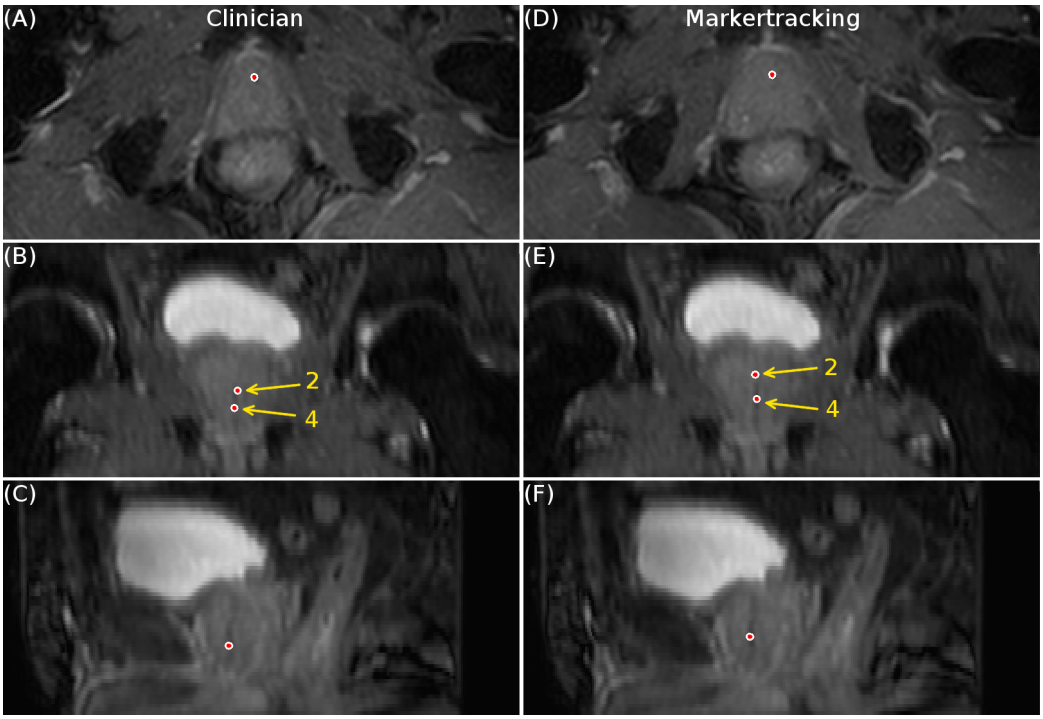

Figure 9: Overview of one cine-MR image set with the largest difference of the COM between the manually segmented markers by the clinician and the positions found by the marker tracking algorithm. Image A-D, B-E and C-F show the respective axial, coronal and sagittal slices of a patient at the end of an imaging session. The marker positions found by the clinician are provided in images A, B and C, while the marker tracking positions are provided in images D, E and F. In this Figure, the middle of the fiducial marker is indicated by the dot, as found by the clinician or marker tracking algorithm. The arrows in image B and E show the position of markers number 2 and 4. The marker shown in image A, D, C and F is labeled with number 4, corresponding to Figure 10.

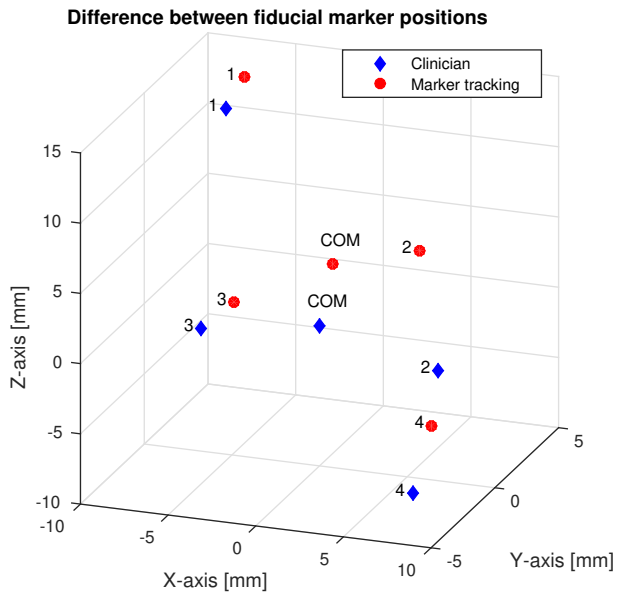

Figure 10: A 3D model of the markers and the center of mass (COM) from the case with the largest difference in the COM between the manually segmented markers by the clinician (diamonds) and the positions found by the marker tracking algorithm (circles). All markers are numbered and have the same numerical labels as shown in Figure 9.